Z-Site Substitution-Driven Transition From Semiconducting Antiferromagnetism to Half-Metallic Ferromagnetism in FeCrRuSi and FeCrRuP Heusler Alloys

R. Lardjani[a,b], R. Baghdad[a,*] and A. Zaoui[b]

[a] *Physics Department, Matter Sciences Faculty, Ibn Khaldoun University of Tiaret, Algeria*
[b] *Computational Materials Physics Laboratory, Djillali Liabès University of Sidi Bel-Abbès, Sidi*

Received: 13.12.2025 & Accepted: 21.01.2026

Doi: 10.12693/APhysPolA.149.25 *e-mail: r_baghdad@univ-tiaret.dz

We report a first-principles density functional theory study employing a modified Becke–Johnson potential of the quaternary Heusler alloys FeCrRuSi and FeCrRuP crystallizing in the Y-type (I) structure. At its equilibrium lattice parameters, FeCrRuSi is predicted to be a semiconducting antiferromagnet, exhibiting an indirect band gap of $\sim$ 0.69 eV in both spin channels, with the Fermi level located just above the valence-band maximum, indicative of weak n-type character. In sharp contrast, FeCrRuP displays robust half-metallic ferromagnetism, characterized by a metallic majority-spin channel and a minority-spin indirect gap of $\sim$ 0.72 eV, resulting in 100% spin polarization at the Fermi level. This pronounced change in electronic and magnetic behavior is attributed to a weakening of the d–p hybridization induced by the Z-site substitution. Replacing Si with P leads to a slight lattice expansion, reducing the covalent interactions between the main-group p states and the transition-metal d orbitals. Projected density-of-states analyses reveal that the minority-spin gap in FeCrRuP originates from strong hybridization between P $3p$ states and transition-metal d states, whereas FeCrRuSi shows a more balanced p–d contribution, consistent with antiferromagnetic order. These results demonstrate that Z-site substitution is an effective route to engineer magnetic order and half-metallicity, identifying FeCrRuP as a promising candidate for spintronic applications.

topics: FeCrRuP, quaternary Heusler, electronic structure, half-metallicity

1. Introduction

The continuous advancement of multifunctional devices in electronics, magnetism, semiconductors, and spintronics necessitates the discovery and development of novel materials that exhibit a broad spectrum of tunable physical properties. In this context, quaternary Heusler alloys (QHAs) with the general chemical formula XX'YZ, where Z is a main-group element and X, X', and Y are transition metals, have emerged as particularly promising candidates. Due to their flexible atomic arrangements, diverse chemical compositions, and rich electronic configurations, QHAs exhibit a wide range of remarkable functional characteristics, including high spin polarization, tunable band gaps, robust ferromagnetism, and good structural stability. These features make the quaternary Heusler alloys highly attractive for next-generation spintronic, thermoelectric, and multifunctional electronic applications [1–5].

First-principles density functional theory (DFT) has proven to be a powerful and reliable approach for predicting and understanding the structural, electronic, magnetic, and transport properties of Heusler-type materials. In particular, Saidi et al. [6] conducted a comprehensive DFT study of full-Heusler X_2TaSi alloys using the full-potential linearized augmented plane wave (FP-LAPW) method combined with the Tran–Blaha modified Becke–Johnson (TB-mBJ) exchange–correlation potential, revealing half-metallic ferromagnetic behaviour and providing detailed insight into the electronic structures. Similarly, Addou et al. [7] employed FP-LAPW calculations to investigate the structural, electronic, optical, and thermoelectric properties of half-Heusler XPdBi compounds, demonstrating the strong predictive capability of first-principles methods to accurately describe both electronic and transport characteristics.

Further studies emphasize the broad versatility of Heusler-family compounds. Czarnacka et al. [8] examined the structural and magnetic properties of full-Heusler Fe_2CrSi and Co_2FeAl alloys using Mössbauer spectroscopy, confirming the structural stability and long-range magnetic ordering of these alloys. In addition, Raj et al. [9] explored the thermoelectric performance of Heusler-based systems, highlighting their potential in efficient energy conversion applications.

Because of their unique ability to host half-metallic or spin-gapless semiconducting behaviour, quaternary Heusler compounds enable nearly 100% spin-polarized currents, high Curie temperatures, and magnetic moments that obey the Slater–Pauling rule; these are in fact key requirements for magnetic tunnel junctions, spin injectors, and magnetoresistive sensors [10–12]. The versatile electronic structures of QHA can be finely tailored by selective substitution at any of the X, Y, or Z atomic sites, allowing precise engineering of electronic, magnetic, and transport characteristics to optimize device performance [13–16].

Structurally, QHAs crystallize in the LiMgPdSn-type (Y-type) structure with cubic space group $F\bar{4}3m$ (no. 216), where the transition metals from the $3d$, $4d$, and $5d$ series occupy distinct Wyckoff positions. Such chemical ordering enables the stabilization of half-metallicity and large magnetic moments through strong d–d and d–p hybridization effects [17]. Notably, the integration of heavy $4d/5d$ elements enhances the spin–orbit coupling, thereby influencing the magneto–electronic behaviour and anisotropy.

In addition to their established spintronic performance, Heusler compounds have recently emerged as efficient thermoelectric materials, owing to their inherently low lattice thermal conductivity and high power factors [18, 19]. Their relatively complex crystalline structures, incorporating heavy atoms with diverse masses, promote phonon scattering and reduce lattice heat transport. The figure of merit (ZT), a critical indicator of thermoelectric efficiency, can thus be enhanced by tuning the electronic band structure and defect engineering. Consequently, rational substitution of constituent atoms, such as replacing Si with P in FeCrRuZ (Z = Si, P), provides a powerful means to simultaneously optimize electronic and phonon transport properties for eco-friendly and high-efficiency thermoelectric applications [20–22].

Recent investigations have reported that Fe- and Ru-based Heusler alloys exhibit stable half-metallic behaviour and high spin polarization. For instance, FeRuCrZ (where Z = Si, Ge) and CoFeMnSi are known to follow Slater–Pauling behaviour, presenting integer magnetic moments and distinct semi-metallic gaps, both experimentally and theoretically [21, 23]. Compounds such as FeRhCrSi and FeCrRuSi further demonstrate mechanical and thermodynamic stability combined with integer magnetic moments hallmarks of complete spin polarization, and potential for practical spintronic deployment [22–24]. However, in the case of FeCrRuSi, Guo et al. [25] report a spin-gapless semiconducting state assuming an ideal, fully ordered quaternary Heusler structure. While this provides an important reference, the influence of subtle atomic rearrangements and near-degenerate configurations is not explicitly addressed. The present work revisits this aspect to assess the stability of the predicted electronic character under more realistic structural conditions.

In this work, we focus on the quaternary Heusler alloys FeCrRuZ (where Z = Si, P), which uniquely integrate a $3d$ element (Cr), renowned for its strong exchange interactions, with a $4d$ element (Ru), known for enhancing spin–orbit coupling and electronic complexity. The substitution between Si (a metalloid) and P (a nonmetal) provides a controlled mechanism to tune the Fermi-level electronic states, thereby influencing both spintronic and thermoelectric behaviour. Despite their predicted half-metallic or semi-metallic nature, these $3d$–$4d$-based Heuslers remain largely unexplored experimentally and theoretically.

Therefore, this study employs first-principles density functional theory (DFT) to comprehensively explore the structural, electronic, magnetic, and thermoelectric transport properties of FeCrRuZ alloys (where Z = Si, P). The findings provide valuable insights into the interplay between crystal chemistry, electronic structure, and transport phenomena, offering guidance for the design of new multifunctional materials suitable for next-generation spintronic and energy conversion technologies.

2. Calculation methodology

The structural, electronic, and transport properties of the quaternary Heusler alloys FeCrRuSi and FeCrRuP were systematically investigated using a first-principles DFT method implemented in the WIEN2k code [26]. Structural optimizations were performed employing the Full-Potential Linearized Augmented Plane Wave (FP-LAPW) method within the Perdew–Burke–Ernzerhof generalized gradient approximation, revised for solids (PBEsol-GGA) [27]. To accurately capture the electronic band structure and transport properties, the Tran–Blaha modified Becke–Johnson (TB-mBJ) exchange–correlation potential was applied [28].

The plane-wave basis set in the interstitial region was determined by the cutoff parameter $K_{\max} = 8.0/R_{\mathrm{MT}}$, where R_{MT} denotes the muffin-tin radius. The chosen values of R_{MT} for Fe, Cr, Ru, Si, and P were 2.22, 2.20, 2.30, 2.10, and 2.00 a.u., respectively. Structural relaxations were carried out using a dense mesh of 1000 irreducible k-points in the first Brillouin zone, with self-consistent field (SCF) convergence achieved when the total energy changed by less than 1×10^{-6} eV/atom. Thermoelectric transport coefficients were evaluated using the BoltzTraP code [29], which solves the semi-classical Boltzmann transport equation in the constant relaxation time approximation (CRTA). Calculations were performed on a fine 20000 k-point mesh, assuming a carrier concentration of 10^{22} cm^{-3} for temperatures of 300, 600, and 900 K.

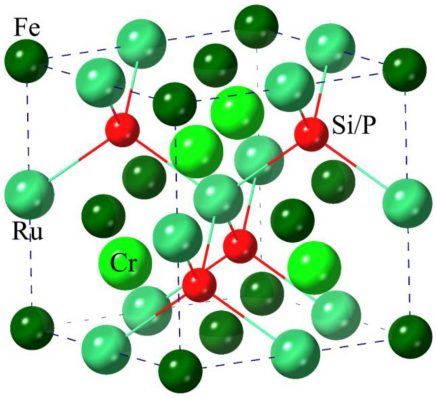

Fig. 1. Crystal structure of the Y-type (I) quaternary Heusler compounds FeRuCrX (X = Si, P).

TABLE I

Optimized crystal structures and corresponding Wyckoff atomic positions for quaternary Heusler alloys FeCrRuX (X = Si, P).

Type	Wyckoff atomic positions			
	4a $(0,0,0)$	4c $(\frac{1}{4},\frac{1}{4},\frac{1}{4})$	4b $(\frac{1}{2},\frac{1}{2},\frac{1}{2})$	4d $(\frac{3}{4},\frac{3}{4},\frac{3}{4})$
Y-I	Fe	Cr	Ru	Si/P
Y-II	Fe	Ru	Cr	Si/P
Y-III	Cr	Fe	Ru	Si/P

This methodology ensures a reliable and high-precision description of both the ground-state properties and the temperature-dependent transport behaviour of these quaternary Heusler alloys.

3. Results and discussions

3.1. Structural properties

The quaternary Heusler alloys FeCrRuSi and FeCrRuP crystallize in the LiMgPdSn-type (Y-type) structure with the space group $F\bar{4}3m$ (no. 216), as shown in Fig. 1. This structure allows three distinct atomic configurations: Y-I, Y-II, and Y-III; they differ by the specific occupation of the four Wyckoff positions (4a, 4b, 4c, 4d). The atomic configurations used in this study are summarized in Table I.

Because even small deviations from the structural order can significantly modify the electronic, magnetic, and transport properties [4], full structural optimization was performed for all possible Y-type variants. The optimization process was conducted by varying the unit-cell volume to minimize the total energy, thereby determining the equilibrium lattice constant, bulk modulus, and ground-state phase of each alloy. Calculations were carried out within the spin-polarized GGA-PBE formalism [27], and the resulting total-energy versus volume curves are presented in Fig. 2a.

Among the three possible Y-type configurations, Y-I exhibits the lowest total energy, indicating it as the most stable structure for both FeCrRuSi and FeCrRuP. The higher energies of the Y-II and Y-III configurations are attributed to unfavorable atomic exchanges that disturb the local chemical order [16].

To verify the magnetic ground state, the total energies of the configurations:

- non-magnetic (NM) — all atomic spins are constrained to zero);
- ferromagnetic (FM) — all atomic spins align parallel in all sublattices);
- ferrimagnetic (FiM) — spins align antiparallel between sublattices, but with unequal moments, giving a non-zero total moment; and
- antiferromagnetic (AFM) — spins align antiparallel with equal magnitude, giving a total moment of zero (fully compensated);

were calculated as a function of volume. The energy–volume relations shown in Fig. 2b reveal that the FM configuration is the most stable for FeCrRuP, whereas FeCrRuSi favors AFM ordering along the (111) direction. The equilibrium parameters were extracted by fitting the Birch–Murnaghan equation of state [30].

The optimized lattice constants were found to be $a = 5.720$ Å for FeCrRuSi and $a = 5.702$ Å for FeCrRuP (Table II), indicating a slightly larger lattice parameter for the Si-based compound, consistent with the larger covalent radius of Si compared to P. Similar trends have been reported for other quaternary Heusler systems, where substitution of main-group elements with larger atomic radii leads to the lattice expansion and a reduced bulk modulus [31–33].

No experimental data are yet available for FeCrRuSi and FeCrRuP; however, the computed results are in excellent agreement with first-principles predictions for related Heusler compounds based on Ru and Fe–Cr [16, 34, 35]. These findings confirm the structural stability of the LiMgPdSn-type phase and the reliability of the computational approach employed in this work.

3.2. Chemical stability

To assess the chemical stability of the quaternary Heusler compounds FeCrRuSi and FeCrRuP, both the cohesive energy and formation enthalpy were computed. These energetic parameters provide fundamental insights into the thermodynamic feasibility and bonding strength of materials.

The cohesive energy E_{Coh} quantifies the energy required to dissociate a compound into its isolated constituent atoms, thus representing the overall strength of interatomic bonds within the crystal

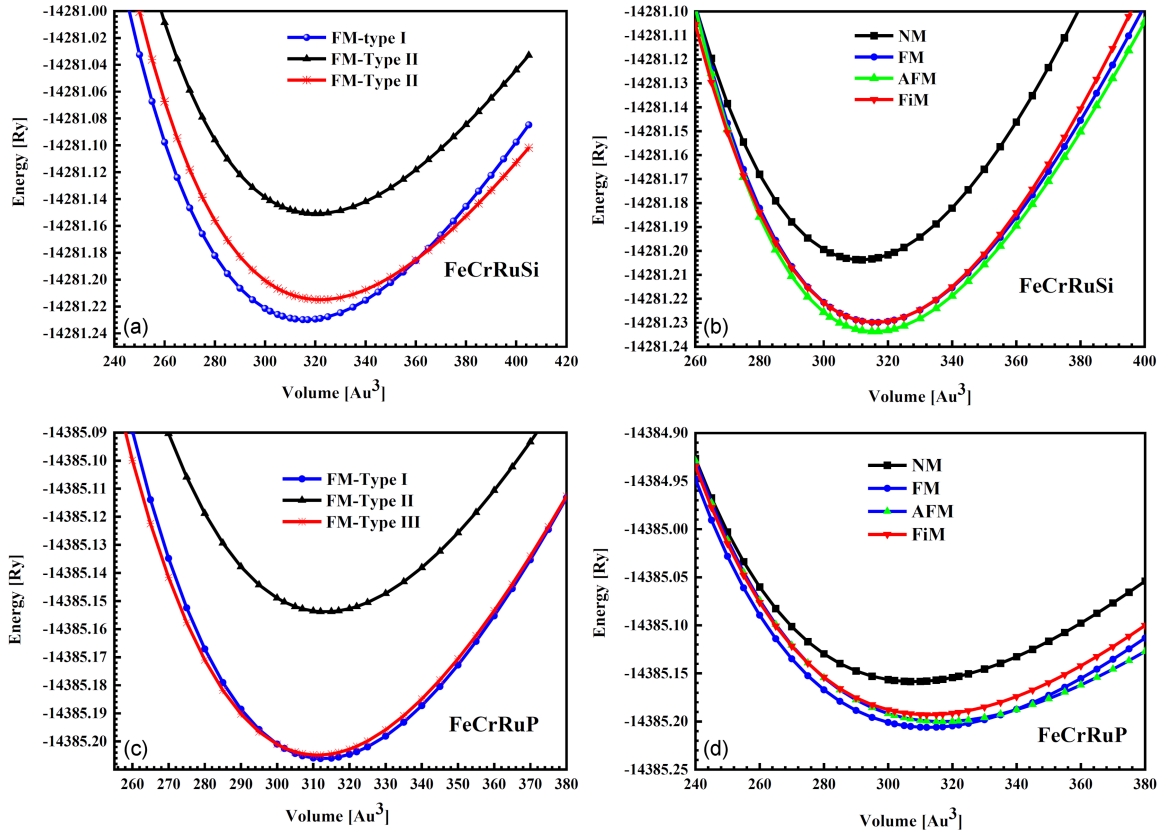

Fig. 2. Total energy as a function of unit-cell volume for (a–b) FeCrRuSi and (c–d) FeCrRuP alloys.

lattice. Conversely, the formation enthalpy ΔH^F measures the energy change accompanying the synthesis of a compound from its most stable elemental phases under standard conditions. These quantities are calculated per formula unit according to the following relations

$$E_{Coh}^{(\mathrm{f.u.})} = E_{tot} - \left(E_{\mathrm{atom}}^{\mathrm{Fe}} + E_{\mathrm{atom}}^{\mathrm{Cr}} + E_{\mathrm{atom}}^{\mathrm{Ru}} + E_{\mathrm{atom}}^{\mathrm{Si/P}}\right), \quad (1)$$

$$\Delta H_{\mathrm{FeCrRuSi/P}}^{F\,(\mathrm{f.u.})} = E_{tot} - E_{\mathrm{solid}}^{\mathrm{Fe}} - E_{\mathrm{solid}}^{\mathrm{Cr}} - E_{\mathrm{solid}}^{\mathrm{Ru}} - E_{\mathrm{solid}}^{\mathrm{Si/P}}. \quad (2)$$

Here, E_{tot} denotes the total energy of the unit cell; $E_{\mathrm{atom}}^{\mathrm{x}}$ are the total energies of the isolated atoms (x = Fe, Cr, Ru, Si, P) in their free states; and $E_{\mathrm{solid}}^{\mathrm{x}}$ represent the per-atom energies of the corresponding elements in their most stable crystalline forms. All calculations were performed using spin-polarized configurations to ensure accurate electronic occupation of the atomic states.

The computed values of cohesive energies and formation enthalpies are summarized in Table II. Both obtained values ($E_{Coh} = -22.45$ eV and $\Delta H^F = -1.87$ eV for FeCrRuSi; $E_{Coh} = -25.28$ eV and $\Delta H^F = -2.68$ eV for FeCrRuP) are negative, indicating that the formation processes are exothermic. In other words, energy is released during the formation of these compounds, suggesting that the interatomic bonds are energetically favorable and that the systems are thermodynamically stable. Our results are consistent with previous first-principles investigations of Heusler-type systems, where similarly negative formation energies were reported, confirming robust thermodynamic stability and strong covalent–metallic bonding characteristics [22, 36].

3.3. Mechanical stability

The mechanical properties of the quaternary Heusler compounds FeCrRuZ (Z = Si, P) were systematically evaluated by first-principles density functional theory (DFT) calculations, with the derived elastic constants and moduli summarized in Table III. The computed elastic tensors are positive definite and fully satisfy the Born–Huang mechanical stability criteria for cubic systems formulated by Mouhat and Coudert [37]. The bulk moduli B of 271 GPa for FeCrRuSi and 245 GPa for FeCrRuP indicate substantial resistance to isotropic compression, reflecting the robust interatomic bonding networks inherent to these alloys. The slightly higher B value for FeCrRuSi correlates with its reduced lattice constant and increased charge-density overlap between transition-metal and main-group atoms, confirming stronger cohesive interactions.

TABLE II

Calculated structural parameters of the quaternary Heusler alloys FeCrRuZ (where Z = Si, P) in different magnetic configurations, namely nonmagnetic (NM), ferromagnetic (FM), ferrimagnetic (FiM), and antiferromagnetic (AFM) phases, together with the computed cohesive energies (E_{Coh}) and formation enthalpies (ΔH^F).

Alloys	Phase	E_{tot} [Ry]	a [Å]	B_0 [GPa]	B_p	E_{Coh} [eV]	ΔH^F [eV]
FeCrRuSi	NM	−14281.20	5.695 5.735[a]	279.84	3.49	−22.45	−1.87
	FM	−14281.23	5.722 5.76[b]	270.93	4.59		
	FiM	−14281.23	5.722 5.76[a]	270.92	4.77		
	AFM	−14281.23	5.72	272.81	5.06		
FeCrRuP	NM	−14385.16	5.672	276.87	4.98	−25.28	−2.68
	FM	−14385.20	5.701	272.58	4.67		
	FiM	−14385.19	5.726 5.74[c]	244.92	5.04		
	AFM	−14385.20	5.716	249.79	4.96		

[a]Ref. [22]; [b]Ref. [33]; [c]Ref. [36].

The calculated Young's moduli ($E = 323$ GPa for FeCrRuSi and $E = 301$ GPa for FeCrRuP) suggest that FeCrRuSi possesses greater intrinsic stiffness, though both compounds remain within the typical stiffness regime of metallic Heusler systems (250–330 GPa). The bulk-to-shear modulus ratios (B/G = 2.12–2.18) surpass the critical Pugh threshold of 1.75, confirming the ductile nature and suitability for mechanical processing or thin-film growth without the risk of brittle failure. Poisson's ratios ($\nu \approx 0.285$–0.288) further corroborate metallic bonding with a moderate degree of angular covalency. The computed Zener anisotropy factors ($\sim$ 1.5) denote moderate elastic anisotropy, implying directional dependence of shear deformation — a characteristic advantageous for strain relaxation during epitaxial integration in spintronic heterostructures.

Substituting Si with P leads to a discernible softening of the mechanical response, as reflected by the $\approx$ 9–10% reduction in the bulk modulus (B), shear modulus (G), and Young's modulus (E). This softening is mainly governed by the larger covalent radius of P and the consequent modification of the p–d hybridization, rather than by electronegativity effects, since P (2.19) is slightly more electronegative than Si (1.90). The altered orbital overlap reduces bond stiffness while maintaining overall elastic stability. Such chemically driven tuning of mechanical properties offers an effective strategy for optimizing lattice matching, alleviating internal stresses, and enhancing strain tolerance in Heusler-based device architectures.

These findings are in strong agreement with the systematic trends described by Tie Yang et al. [38], who established that the elastic response in Heusler alloys scales with the bonding strength and atomic size of the main-group element. Likewise, the predicted elastic stiffness for FeCrRuSi closely aligns with the DFT values reported by Wang et al. [22], with discrepancies confined to the expected range of ±10% due to methodological and lattice-parameter variations. Collectively, the combination of high stiffness ($B \approx 250$–270 GPa), pronounced ductility ($B/G > 2$), and moderate anisotropy underscores the mechanical resilience of

TABLE III

The summarized values of: elastic constants C_{ij}, bulk modulus B, shear modulus G, Young modulus E, Poisson ratio ν, Vickers hardness H, the universal anisotropy index A_U, and the Zener anisotropy A. (Units of these paramters are in GPa, except for ν, A and A_U).

Property	FeCrRuSi		FeCrRuP
	This work	Other works[a]	This work
C_{11}	382.0	361.1	356.0
C_{12}	165.0	181.9	186.0
C_{44}	148.0	141.6	138.0
B	271.0	241.6	245.0
G	124.5	121.9	115.8
E	322.7	239.1	301.4
ν	0.285	–	0.288
H	5.05	–	3.86
A_U	0.117	–	0.287
A	1.49	1.60	1.53
B/G	2.18	1.98	2.12

[a]Ref. [22]

FeCrRuSi and FeCrRuP. This establishes them as promising candidates for spintronic and magneto–electronic applications requiring exceptional structural robustness and strain-tolerant performance.

3.4. Magnetic properties

The magnetic behavior of quaternary Heusler alloys is a key factor determining their suitability for spintronic and magneto–electronic applications, since control of spin polarization and magnetic compensation directly affect device performance. In the present investigation, the total and atomic magnetic moments of FeCrRuP and FeCrRuSi were evaluated to elucidate their spin configurations and electronic–magnetic correlations. The calculated total and atomic magnetic moments are summarized in Table IV. The calculated total magnetic moment of FeCrRuP is $\mu_{tot} \approx 3\mu_B$ per formula unit (e.g., FeCrRuP exhibits a FM alignment with $\mu_{\mathrm{Fe}} \approx +1.67\mu_{\mathrm{B}}$, $\mu_{\mathrm{Cr}} \approx +1.25\mu_{\mathrm{B}}$, and $\mu_{\mathrm{Ru}} \approx -0.05\mu_{\mathrm{B}}$, giving $\sim 3\mu_{\mathrm{B}}$ per formula unit), confirming a ferromagnetic ground state and an integer moment consistent with half-metallic ferromagnetism. In the FM state of FeCrRuSi, the atomic magnetic moments are $\mu_{\mathrm{Fe}} \approx +1.26\mu_{\mathrm{B}}$, $\mu_{\mathrm{Cr}} \approx +1.03\mu_{\mathrm{B}}$, and $\mu_{\mathrm{Ru}} \approx -0.31\mu_{\mathrm{B}}$, leading to a total moment close to $2\mu_{\mathrm{B}}$. In contrast, in the AFM configuration, the Fe and Cr sublattices reverse their spin orientations, resulting in $\mu_{\mathrm{Fe}} \approx +1.22\mu_{\mathrm{B}}$, $\mu_{\mathrm{Cr}} \approx -1.22\mu_{\mathrm{B}}$, and $\mu_{\mathrm{Ru}} \approx 0\mu_{\mathrm{B}}$. This perfect compensation yields a net moment of zero, indicating a transition toward a fully compensated half-metallic ferrimagnetic state. Such magnetic behaviour perfectly obeys the Slater–Pauling rule, $M_{tot} = Z_{tot} - 24$, which correlates the total magnetic moment (M_{tot}) with the total number of valence electrons (Z_{tot}); this rule has been extensively verified for half-metallic Heusler systems [39].

An additional factor contributing to the different magnetic ground states of FeCrRuSi and FeCrRuP is the valence-electron count, since P provides one valence electron more than Si. This extra electron increases Z_{tot}, leading to enhanced filling of the transition-metal d states, particularly in the majority-spin channel. As a result, the exchange splitting is reinforced and the ferromagnetic alignment in FeCrRuP is stabilized, yielding an integer magnetic moment in full agreement with the Slater–Pauling rule. In contrast, the lower valence-electron count in FeCrRuSi favors antiferromagnetic Fe–Cr exchange interactions, resulting in a compensated magnetic state.

Our computed moments are in excellent agreement with previous first-principles predictions for similar Ru-containing compounds. For example, Ma et al. [36] reported a total magnetic moment for FeRuCrP of $3\mu_B$, confirming its half-metallic nature and full compliance with the Slater–Pauling relation; likewise, Wang et at. [22] demonstrated

TABLE IV

Calculated total (per formula unit) and atomic magnetic moments (μ_{B}) for the quaternary Heusler alloys FeCrRuSi (AFM order) and FeCrRuP (FM order).

Alloys	μ_{Fe}	μ_{Cr}	μ_{Ru}	$\mu_{\mathrm{Si/P}}$	μ_{int}	μ_{tot}
FeCrRuSi	1.26	1.03	−0.31	−0.01	0.09	~ 2.00
FeCrRuP	1.67	1.25	−0.05	0.02	0.12	~ 3.00

that FeCrRuSi exhibits a $2\mu_{\mathrm{B}}$ moment in the ferromagnetic state with a minority-spin gap of about 0.384 eV, arising from strong Fe–Cr–Ru d–p hybridization. Comparable integer-moment behaviour has been observed in CoFeMnSi and MnCrRuAl, confirming that the total moment is primarily governed by the valence-electron count and the exchange splitting between majority and minority spin channels [13].

The incorporation of Ru, a $4d$ element, enhances the delocalization of d electrons and strengthens the exchange coupling between Fe and Cr sublattices, stabilizing ferromagnetism while maintaining high spin polarization, as also reported by Bainsla et al. [21] for Ru-based Heuslers. The zero-moment antiferromagnetic ground state predicted for FeCrRuSi places it in the same functional class as experimentally realized compensated ferrimagnetic Heuslers such as Mn_2RuXGa, which exhibit vanishing macroscopic magnetization yet retain complete spin polarization at the Fermi level [40]. Such materials eliminate stray magnetic fields while allowing ultrafast spin dynamics, making these materials ideal for antiferromagnetic spintronic memory and logic devices. Therefore, the results obtained here confirm that FeCrRuP behaves as a half-metallic ferromagnet with a stable integer moment following the Slater–Pauling rule, whereas FeCrRuSi undergoes a ferromagnetic-to-compensated-antiferromagnetic transition controlled by Fe–Cr exchange interactions and Ru-mediated hybridization. This dual magnetic nature, combining half-metallicity and magnetic compensation, highlights the technological potential of FeCrRuSi as a prototype compound for next-generation low-stray-field and energy-efficient spintronic architectures.

3.5. Electronic properties

We computed the spin-polarized electronic band structures and density of states (DOS) of the quaternary Heusler alloys FeCrRuSi and FeCrRuP using the modified Becke–Johnson (TB-mBJ) potential at their respective equilibrium lattice parameters in the Y-type (I) configuration. Although both compounds crystallize with the same symmetry,

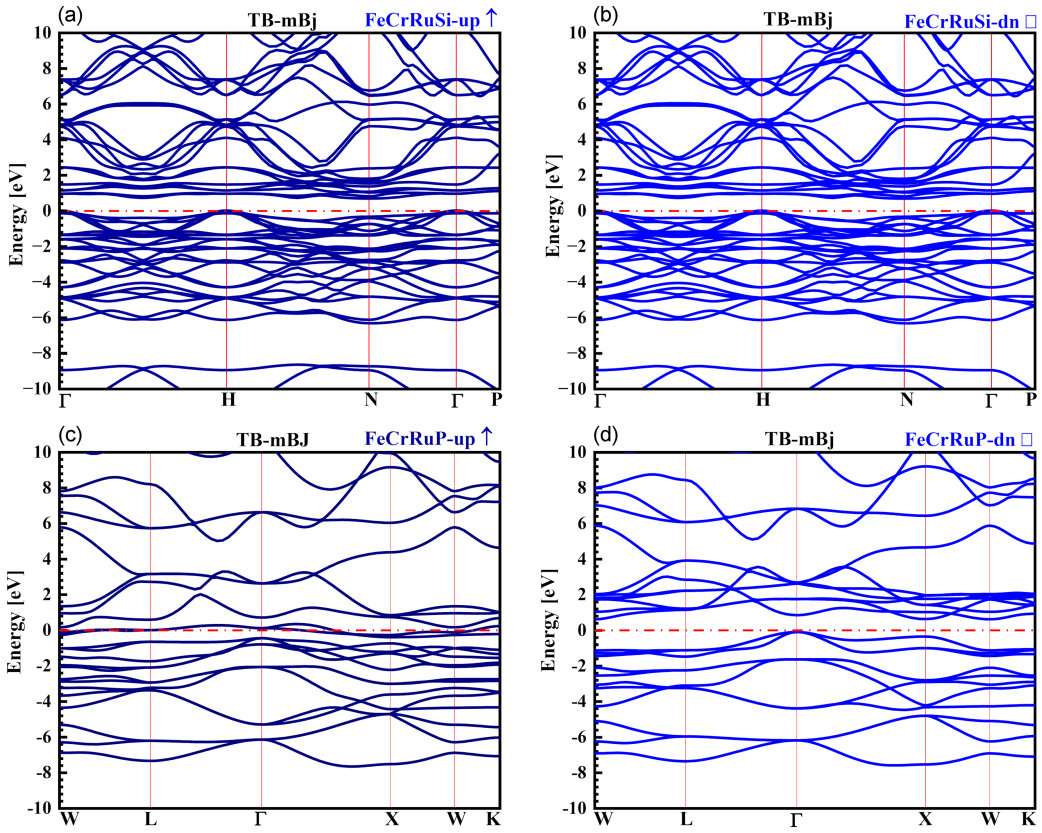

Fig. 3. Spin-resolved electronic band structures of (a–b) FeCrRuSi and (c–d) FeCrRuP alloys, calculated using the TB-mBJ approximation. The Fermi level is fixed at 0 eV.

their electronic and magnetic ground states differ sharply, depending on whether the main-group element is Si or P — this distinction strongly influences lattice constant, orbital overlap, and the strength of the *d–p* hybridization.

In the case of FeCrRuSi, the dispersion in the spin-up and spin-down bands is nearly symmetric. In both spin channels, we found an *indirect* band gap of approximately 0.69 eV along the Γ–N direction. The Fermi level lies just above the valence-band maximum (VBM), implying weak n-type behaviour and confirming a semiconducting antiferromagnetic (SC–AFM) ground state. Neither spin channel exhibits metallic behaviour, clearly distinguishing FeCrRuSi from its phosphide analog.

In contrast, FeCrRuP exhibits a markedly asymmetric spin-resolved band structure (Fig. 3). The majority-spin (↑) channel is metallic, with multiple bands crossing the Fermi level (E_F), whereas the minority-spin (↓) channel shows an indirect band gap of roughly 0.72 eV along the Γ–W path. This strong spin asymmetry is the hallmark of half-metallicity, classifying FeCrRuP as a half-metallic ferromagnet (HM-FM), in full agreement with the classical half-metallic Heusler model first introduced by de Groot et al. [12] (1983), and later validated in numerous quaternary Heusler compounds [13].

The transition in electronic behavior induced by Z-site substitution (Si → P) can be rationalized by orbital hybridization arguments. Although P has a smaller atomic radius than Si, replacing Si with P paradoxically slightly *expands* the lattice. This expansion arises from weaker bonding and reduced covalency, which in turn reduces *d–p* hybridization between the transition-metal (Fe, Cr, Ru) *d* states and the main-group *p* states. Consequently, in FeCrRuP, the majority-spin conduction bands become sufficiently delocalized to cross the Fermi energy E_F, while the minority-spin channel retains a finite gap. This mechanism, which underlies the emergence of half-metallicity, parallels trends observed in other quaternary Heusler alloys (see, e.g., Ram et al. [41] (2020)).

The total and projected DOS (Fig. 4) further elucidate these behaviors. In FeCrRuP, the minority-spin gap stems from hybridization between P-3*p* orbital and Fe/Cr/Ru-*d* orbital. Meanwhile, the metallic majority-spin states at E_F are dominated by contributions from Fe-3*d*, Cr-3*d*, and Ru-4*d*. In the bonding region between −2 and −1 eV (below E_F), strong *d–d* coupling among the transition metals prevails; above E_F (around +0.8 eV), antibonding *d–p* interactions enhance delocalization and help stabilize ferromagnetism. This distribution with bonding *d–d* states below and

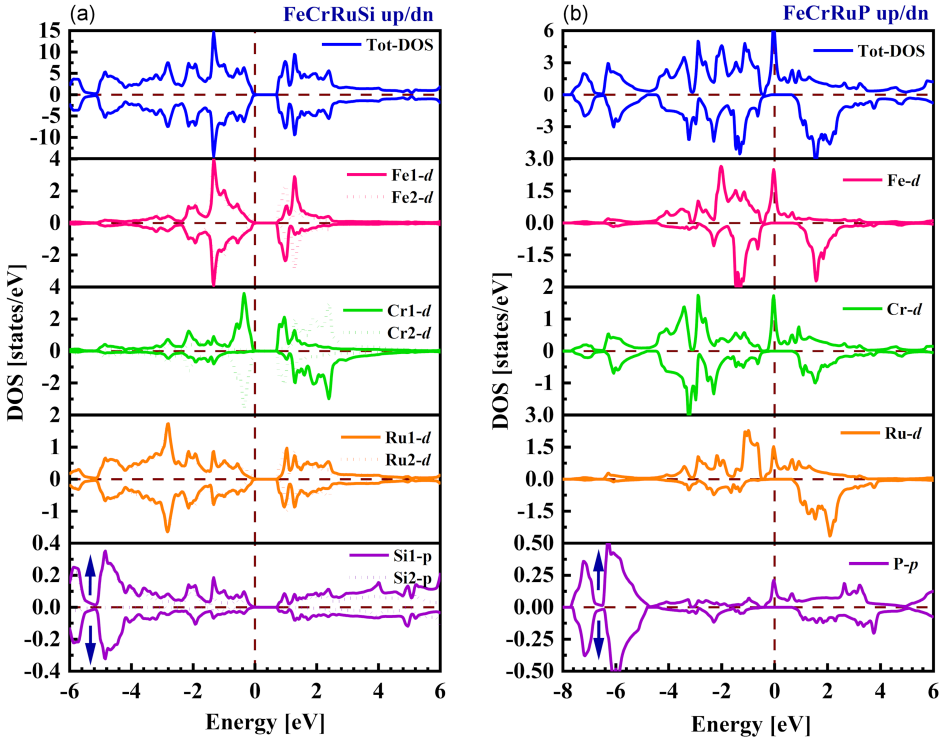

Fig. 4. Spin-polarized density of states (DOS) for FeCrRuSi (a) and FeCrRuP (b) alloys, calculated using the TB-mBJ approximation. The Fermi level is fixed at 0 eV.

antibonding states d–p above E_F typifies half-metallic Heuslers (e.g., Ghosh et al. [42] (2019)).

In the case of FeCrRuSi, DOS analysis reveals that the conduction band is primarily composed of Si-3p and Ru-4d orbitals, while the valence band is dominated by Fe-3d and Cr-3d states. The reduced d–p coupling correlates with the larger band gap and semiconducting behaviour. Near the valence-band maximum, the dominant contributions arise mainly from the Fe-1 and Cr-1 states, while the states Fe-2 and Cr-2 are shifted towards lower energies, consistent with the exchange splitting characteristic of the antiferromagnetic ordering. The two inequivalent Si sites (Si-1 and Si-2) provide complementary p-state contribution near the conduction-band minimum (CBM), promoting structural stability and charge homogeneity — a feature also observed in Heusler semiconductors such as CoFeMnSi (see Xu et al. [43] (2013)).

Taken together, a comparison between FeCrRuP and FeCrRuSi reveals a clear electronic–magnetic phase transition driven by substitution at the Z site. As the p orbital of the main-group element becomes more localized (when going from Si to P), the p–d hybridization weakens, the band gap closes in a single spin channel, and concomitantly metallicity appears, and the material transitions from an antiferromagnetic to a ferromagnetic state. This tunability via chemical substitution provides a design principle for tailoring the spintronic functionality of quaternary Heusler compounds [44].

From an application perspective, FeCrRuP — with its full spin polarization and metallic behaviour in the majority-spin channel — is a compelling candidate for magnetic tunnel junctions and spin-filter devices. Meanwhile, FeCrRuSi, due to its semiconducting nature and spin-resolved band topology, may be exploited in spin-gapless semiconductors or magnetoresistive sensors. Overall, the strong interplay among lattice parameters, electronic configuration, and magnetic ordering in FeCrRuZ (Z = P, Si) underscores the broader relevance of d–p hybridization engineering in the rational design of Heusler alloys.

Finally, comparing our calculated gaps with previous first-principles studies reveals important distinctions. For FeCrRuP, previous GGA+PBEsol calculations reported a minority-spin indirect gap of ~ 0.354 eV (Ma et al. [36] (2017)), whereas our TB-mBJ-based results yield ≈ 0.72 eV. For FeCrRuSi, earlier GGA+PBEsol calculations gave a gap of around 0.40 eV in both spins, and even reported half-metallicity with a metallic majority channel and a gap of 0.384 eV (Wang et al. [22] (2017)). In contrast, our GGA+TB-mBJ results give a gap of ~ 0.693 eV, indicating semiconducting behaviour. These discrepancies highlight how subtle differences, such as atomic ordering, equilibrium lattice constant, or the choice of exchange–correlation functional, can significantly influence not just the magnitude of the gap but the fundamental spin-dependent character of quaternary Heusler systems.

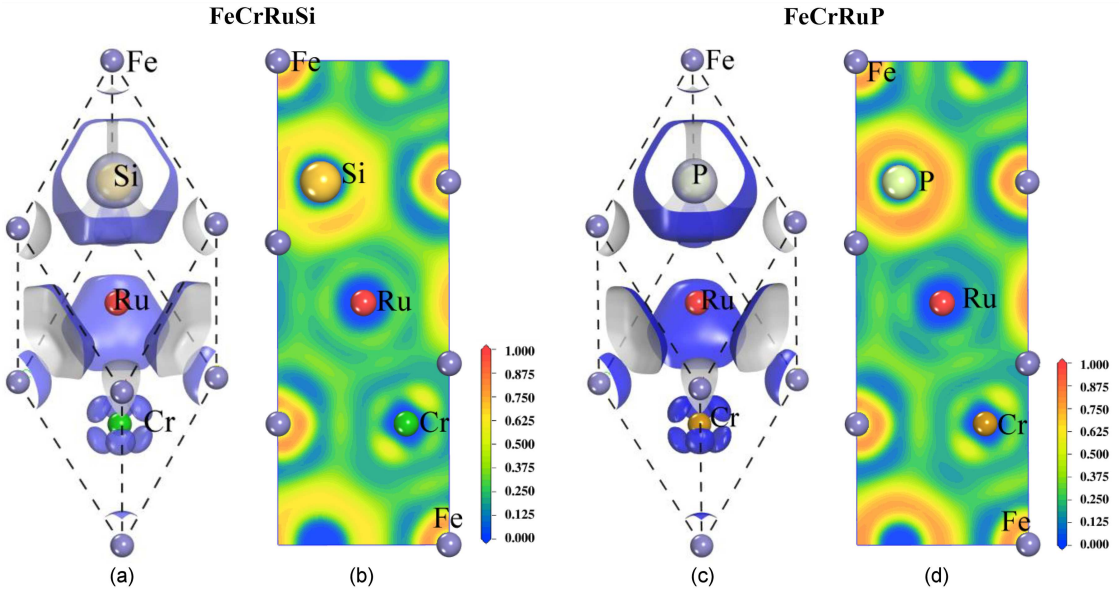

Fig. 5. (a, c) 3D ELF iso-surfaces (ELF = 0.4) showing the valence electron localization for FeCrRuSi and FeCrRuP. (b, d) 2D ELF cross-sectional maps.

3.6. Electron localization function (ELF)

The electron localization function (ELF) provides a quantitative description of electron pairing and localization in solids, reflecting the influence of the Pauli exclusion principle. Originally proposed by Becke and Edgecombe, ELF estimates the likelihood of finding two electrons with parallel spins in close proximity, thereby offering a clear representation of the electronic structure and chemical bonding in materials [45]. Subsequent developments by Savin et al. [46] and Fuster et al. [47] extended the utility of EFT to complex molecular and solid-state systems, making it a reliable indicator of the bonding character in metallic and covalent frameworks.

Figure 5a presents three-dimensional (3D) ELF iso-surfaces (ELF = 0.4) for the FeCrRuSi and FeCrRuP compounds, visualizing regions of electron localization. Two distinct areas of high ELF values are observed — one oriented along the vertical direction and another within the crystallographic plane, revealing anisotropic electron distribution associated with different bonding configurations.

The two-dimensional (2D) ELF maps shown in Fig. 5b provide complementary insights into the bonding nature. Strong electron localization is evident between transition-metal atoms (Fe, Cr, Ru), which corresponds to metallic-type interactions extending into the interatomic regions. The ELF maxima in these regions ($\approx$ 0.6–0.8) indicate the presence of delocalized metallic bonding. Furthermore, noticeable p–d hybridization occurs between the d orbitals of the transition metals and the p orbitals of the main-group element Z (i.e., Si or P), giving rise to the formation of covalent and polar covalent bonds. Around the Fe, Si, and P sites, ELF values typically range from 0.7 to 0.9, signifying localized electron density consistent with covalent character, whereas in the Ru–Cr intermetallic regions, lower ELF values ($\approx$ 0.4–0.5) imply weaker localization and partial metallic bonding.

The substitution of Si by P significantly influences the bonding nature. In FeCrRuSi, the Si–Fe and Si–Cr interactions exhibit stronger covalent character due to the higher degree of sp^3 hybridization and shorter bond distances associated with Si. Conversely, in FeCrRuP, P introduces slightly more polar covalent bonding; its $3p$ orbitals are more localized than those of Si, leading to reduced orbital overlap and, overall, a weaker covalent interaction.

Additionally, differences in the electronegativity among the constituent elements (i.e., 1.83 for Fe, 1.66 for Cr, 2.20 for Ru, 1.90 for Si, 2.19 for P) introduce a minor ionic component to the bonding framework, particularly between the transition-metal atoms and the Z elements. This mixed covalent–ionic–metallic character governs the overall electronic distribution and contributes to the stability of both compounds.

3.7. Thermoelectric properties

Heusler compounds have recently attracted increasing attention for thermoelectric applications due to their high Seebeck coefficients, tunable carrier concentrations, and mechanical robustness [48]. Peculiar electronic states near the Fermi level, often

influenced by intrinsic chemical disorder, offer an efficient way to tailor their thermoelectric behaviour. To investigate these characteristics, the transport coefficients, namely the Seebeck coefficient (S), electrical conductivity (σ), electronic thermal conductivity (κ_e), and the dimensionless figure of merit (ZT), were evaluated using semi-classical Boltzmann transport theory within a constant relaxation time (τ) approximation, as implemented in the BoltzTraP2 code [26, 49].

The main transport quantities are defined as

$$S = \frac{e}{3T\sigma} \int \mathrm{d}\varepsilon \left(-\frac{\partial f}{\partial \varepsilon}\right) \rho(\varepsilon)\, \tau(\varepsilon)\, \nu(\varepsilon)^2\, (\varepsilon - \mu), \tag{3}$$

$$\sigma = \frac{e^2}{3} \int \mathrm{d}\varepsilon \left(-\frac{\partial f}{\partial \varepsilon}\right) \rho(\varepsilon)\, \tau(\varepsilon)\, \nu(\varepsilon)^2, \tag{4}$$

where $\rho(\varepsilon)$ is the density of states (DOS), $f(\varepsilon)$ is the Fermi–Dirac distribution, $\nu(\varepsilon)$ is the carrier velocity, $\tau(\varepsilon)$ denotes the relaxation time, and μ is the chemical potential.

The dimensionless thermoelectric figure of merit is expressed as

$$ZT = \frac{S^2 \sigma}{\kappa_e + \kappa_l}\, T, \tag{5}$$

where κ_e and κ_l are the electronic and lattice contributions to thermal conductivity, respectively. A high values of S and σ combined with a low total thermal conductivity κ are required to achieve superior thermoelectric efficiency [48, 49].

Temperature-dependent and chemical potential-dependent Seebeck coefficients for FeCrRuP and FeCrRuSi were calculated at 300, 600, and 900 K (Fig. 6). Both alloys exhibit similar overall trends in the chemical potential range $-2 \le \mu \le 2$ eV. The sign change of S distinguishes p-type conduction (positive S) from n-type conduction (negative S). The Seebeck coefficient reaches its maximum when the chemical potential deviates slightly from the Fermi level, indicating optimal charge–carrier asymmetry near E_F.

At 300 K, the maximum values of S are $\approx$ 848.3 μV/K for FeCrRuP and 1106.2 μV/K for FeCrRuSi, decreasing to 268.4 μV/K and 137.2 μV/K at 600 K, and to 90.5 μV/K at 900 K, respectively. The higher S values in FeCrRuP result from its narrower band gap, which enhances carrier localization and energy filtering. As the temperature increases, S decreases due to enhanced bipolar conduction and carrier excitation in the gap. Remarkably, the obtained S values are an order of magnitude higher than those reported for other quaternary Heusler alloys [50–52], signifying strong potential for thermoelectric applications.

Figure 7 shows the variation of the normalized electrical conductivity (σ/τ) as a function of $\mu - E_\mathrm{F}$ for both alloys. FeCrRuP exhibits a broader chemical potential region with negligible conductivity compared to FeCrRuSi, which reflects its stronger semiconducting character. In the p-type region, FeCrRuSi shows a more rapid increase in conductivity than FeCrRuP, whereas in the n-type region FeCrRuP dominates.

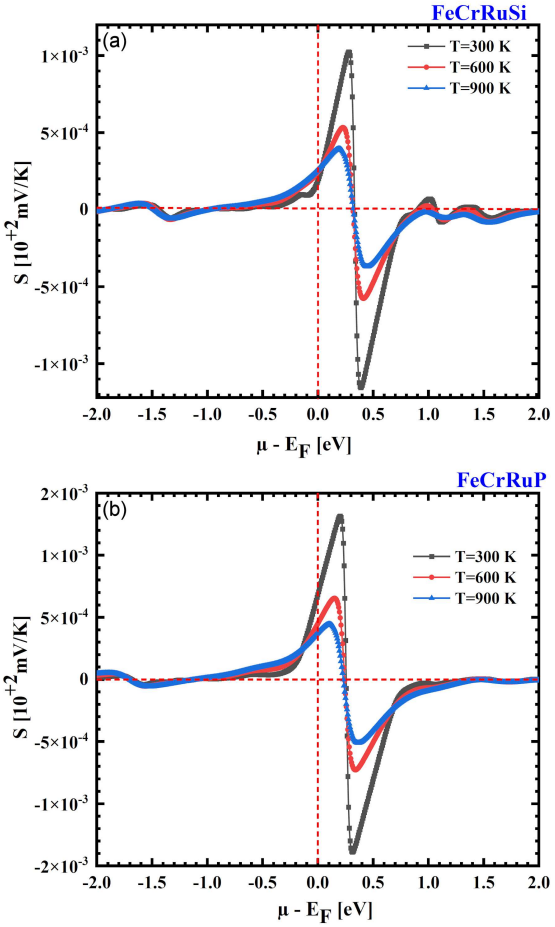

Fig. 6. Seebeck coefficient versus chemical potential for (a) FeCrRuSi and (b) FeCrRuP alloys, at 300, 600, and 900 K.

At 300 K, the maximum p-type conductivity reaches 2.88×10^{20} and 3.39×10^{20} $(\Omega\ \mathrm{m\ s})^{-1}$ at $\mu \approx -1.15$ and -1.12 eV for FeCrRuSi and FeCrRuP, respectively. For n-type carriers, the values are 1.76×10^{20} $(\Omega\ \mathrm{m\ s})^{-1}$ (FeCrRuSi) and 4.11×10^{20} $(\Omega\ \mathrm{m\ s})^{-1}$ (FeCrRuP) at $\mu \approx 1.31$–1.37 eV. The conductivity is nearly temperature-independent, suggesting that the dominant scattering mechanism remains unchanged with heating. Overall, FeCrRuP exhibits enhanced charge–carrier mobility in the n-type regime, underscoring its superior transport behaviour.

The thermoelectric efficiency is related inversely to the thermal conductivity; thus, κ must remain minimal. The total thermal conductivity is given by

$$\kappa = \kappa_e + \kappa_l, \tag{6}$$

where κ_e originates from charge carriers and κ_l from phonons. Since BoltzTraP2 calculates only κ_e, the lattice term was not considered here.

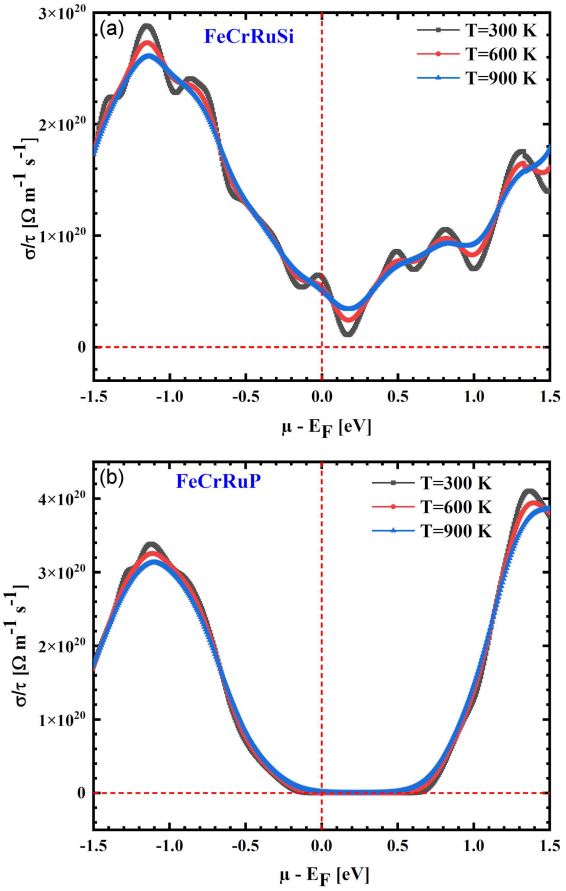

Fig. 7. Electrical conductivity versus chemical potential for (a) FeCrRuSi and (b) FeCrRuP alloys, at 300, 600, and 900 K.

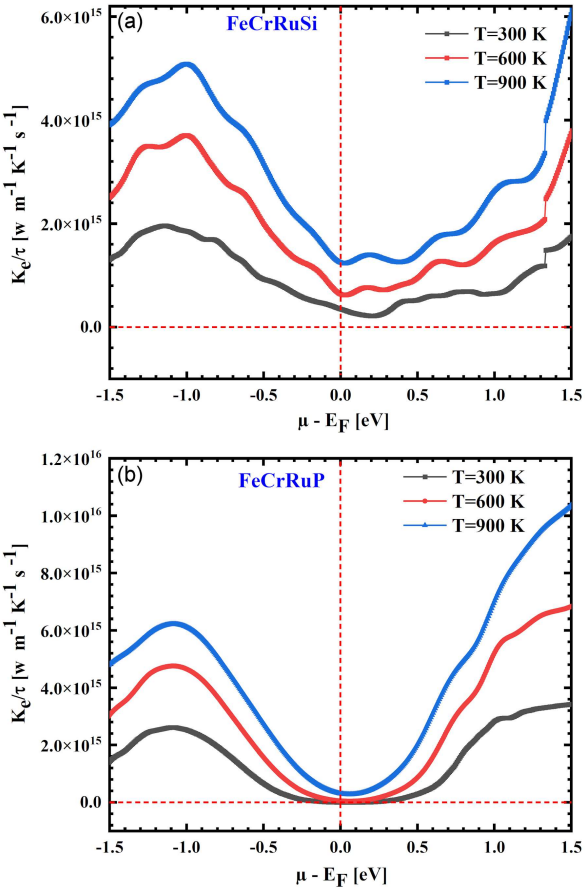

Fig. 8. Thermal conductivity versus chemical potential for (a) FeCrRuSi and (b) FeCrRuP alloys, at 300, 600, and 900 K.

As depicted in Fig. 8, κ_e increases with temperature and $|\mu|$ for both compounds. At 300 K, κ_e is nearly zero near the Fermi level in the p-type region, but rises rapidly at higher values of $|\mu|$, reaching 1.95×10^{15} and 2.61×10^{15} W/(m K s) for FeCrRuSi and FeCrRuP, respectively. Indeed, κ_e/τ increases monotonically in the n-type region and does not exhibit a local maximum. FeCrRuSi consistently exhibits lower κ_e values, indicating superior phonon scattering and the potential for enhanced ZT. Notably, both alloys demonstrate significantly reduced electronic thermal conductivity κ_e compared to the Heusler systems described earlier [21, 35].

The thermoelectric figure of merit ZT serves as a direct measure of the material performance. Materials with $ZT \geq 1$ are generally regarded as efficient thermoelectrics [48]. Computed $ZT(\mu T)$ profiles for FeCrRuP and FeCrRuSi (Fig. 9) reveal two distinct peaks at 300 K. For FeCrRuSi, ZT reaches 0.37 and 0.23 at $\mu = 0.11$ and 0.23 eV, respectively. In contrast, FeCrRuP displays higher peaks of 0.93 and 0.89 at $\mu = -0.03$ and 0.14 eV, respectively. With increasing temperature, ZT decreases slightly due to the increase in thermal conductivity.

Overall, FeCrRuP exhibits a superior thermoelectric response, benefiting from a narrower band gap, a higher Seebeck coefficient, and optimal electrical transport. The performance of this alloy is comparable to that of the recently reported high-efficiency quaternary Heusler systems [53, 54], which positions FeCrRuP as a promising candidate for next-generation thermoelectric device applications, even at room temperature.

4. Conclusions

In summary, our first-principles study using the mBJ potential demonstrates that the substitution at the Z site from Si to P in the quaternary Heusler system FeCrRuZ induces a pronounced electronic–magnetic phase transition. FeCrRuSi is predicted to be a semiconducting antiferromagnet, with a robust indirect band gap of ~ 0.69 eV in both spin channels and the Fermi level just above the valence-band maximum, indicating weak n-type behaviour. In contrast, FeCrRuP exhibits half-metallic ferromagnetism, characterized by a metallic majority-spin channel and a sizable gap

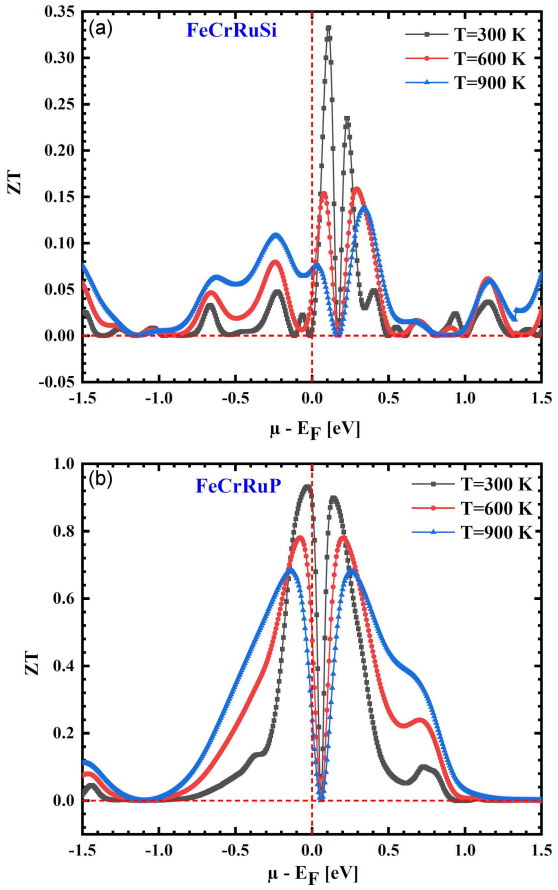

Fig. 9. Figure of merit (ZT) versus chemical potential for (a) FeCrRuSi and (b) FeCrRuP alloys, at 300, 600, and 900 K.

of ~ 0.72 eV in the minority-spin channel, conferring full spin polarization at the Fermi level.

We attribute this transition primarily to a weakening of the d–p hybridization, driven by a subtle lattice expansion when Si is replaced by P. This expansion reduces the covalent bonding between the main-group p-orbitals and the transition-metal d-states, enabling the majority-spin conduction band to cross the Fermi level while preserving a gap in the minority channel. Analysis of the projected density of states confirms that in FeCrRuP, the minority gap originates from coupling between the P-3p and Fe/Cr/Ru-d states, whereas in FeCrRuSi, the conduction (Si-3p, Ru-4d) and valence (Fe-3d, Cr-3d) bands reflect its antiferromagnetic order.

This chemical engineering strategy offers a powerful design principle for tailoring the magnetic and transport properties in quaternary Heusler alloys by fine-tuning the d–p interactions. From an application perspective, FeCrRuP emerges as a strong candidate for spintronic devices (e.g., magnetic tunnel junctions), while FeCrRuSi, with its semiconducting antiferromagnetic character, could be exploited in spin-gapless semiconductors or magnetoresistive sensors.

Looking ahead, experimental synthesis and characterization of these compounds are crucial to validate our predictions. Additionally, further theoretical work may explore the effects of strain, defects, and temperature on the stability of the half-metallic and antiferromagnetic phases, as well as transport properties under realistic device conditions.

Acknowledgments

The authors would like to thank Professor Mohamed Mana (University of Mostaganem, Algeria) for his helpful and insightful discussions regarding the thermoelectric properties of the investigated compounds.

References

[1] Y. Venkateswara, J. Nag, S.S. Samatham, A.K. Patel, P.D. Babu, M.R. Varma, J. Nayak, K.G. Suresh, *Phys. Rev. B* **107**, L100401 (2023).

[2] S. Gupta, S. Chakraborty, V. Bhasin et al., *Phys. Rev. B* **108**, 045137 (2023).

[3] C.K. Barman, C. Mondal, B. Pathak, A. Alam, *Phys. Rev. B* **99**, 045144 (2019).

[4] V. Alijani, S. Ouardi, G.H. Fecher et al., *Phys. Rev. B* **84**, 224416 (2011).

[5] R. Kumar, S. Gupta, *Appl. Phys. Lett* **124**, 022402 (2024).

[6] N. Saidi, W. Benstaali, A. Abbad, S. Bentata, *Acta Phys. Pol. A* **148**, 136 (2025).

[7] O. Addou, A. Touia, K. Benyahia, *Acta Phys. Pol. A* **143**, 252 (2023).

[8] K. Czarnacka, P. Jaskółowska, D. Oleszak, M. Pękała, E. Jartych, *Acta Phys. Pol. A* **146**, 227 (2024).

[9] E. Raj, R. Gozdur, Ł. Bernacki, Ł. Ruta, *Acta Phys. Pol. A* **147**, 209 (2025).

[10] T. Graf, C. Felser, S.S.P. Parkin, *Prog. Solid State Chem.* **39**, 1 (2011).

[11] S. Chadov, X. Qi, J. Kübler, G.H. Fecher, C. Felser, S.C. Zhang, *Nat. Mater.* **9**, 541 (2010).

[12] R.A. de Groot, F.M. Mueller, P.G. van Engen, K.H.J. Buschow, *Phys. Rev. Lett.* **50**, 2024 (1983).

[13] S. Skaftouros, K. Özdoğan, E. Şaşıoğlu, I. Galanakis, *Phys. Rev. B* **87**, 024420 (2013).

[14] C. Fecher, G.H. Felser, B. Balke, *Angew. Chem. Int. Ed.* **46**, 668 (2007).

[15] M. Meinert, J.M. Schmalhorst, G. Reiss, *J. Phys. Condens. Matter* **23**, 116005 (2011).

[16] I.S. Dedov, A.V. Lukoyanov, *Phys. B Condens Matter* **677**, 415736 (2024).

[17] V. Alijani, J. Winterlik, G.H. Fecher, S.S. Naghavi, C. Felser, *Phys. Rev. B* **83**, 184428 (2011).

[18] R. Prakash, G. Kalpana, *RSC Adv.* **13**, 10847 (2023).

[19] C.S. Lue, C.F. Chen, J.Y. Lin, Y.T. Yu, Y.K. Kuo, *Phys. Rev. B* **75**, 064204 (2007).

[20] I. Shigeta, O. Murayama, T. Hisamatsu, A. Brinkman, A.A. Golubov, Y. Tanaka, M. Ito, H. Hilgenkamp, M. Hiroi, *J. Phys. Chem. Solids* **72**, 604 (2011).

[21] L. Bainsla, A.I. Mallick, M.M. Raja, A.K. Nigam, B.S.D.C.S. Varaprasad, Y.K. Takahashi, K. Alam, K.G. Suresh, K. Hono, *Phys. Rev. B* **91**, 104408 (2015).

[22] X. Wang, H. Khachai, R. Khenata et al. *Sci. Rep.* **7**, 16183 (2017).

[23] L.F. Feng, J.N. Ma, Y. Yang, T. Lin, L. Wang, *Appl. Sci.* **8**, 2370 (2018).

[24] Y. Venkateswara, S.S. Samatham, P.D. Babu, K.G. Suresh, A. Alam, *Phys. Rev. B* **100**, 180404(R) (2019).

[25] X. Guo, Z. Ni, Z. Liang, H. Luo, *Comput. Mater. Sci.* **154**, 442 (2018).

[26] P. Blaha, K. Schwarz, G. Madsen, D. Kvasnicka, J. Luitz, "WIEN2k: An Augmented Plane Wave plus Local Orbitals Program for Calculating Crystal Properties", Vienna University of Technology, Vienna 2001.

[27] J.P. Perdew, K. Burke, M. Ernzerhof, *Phys. Rev. Lett.* **78**, 1396 (1997).

[28] D. Koller, F. Tran, P. Blaha, *Phys. Rev. B* **85**, 155109 (2012).

[29] G.K.H. Madsen, D.J. Singh, *Comput. Phys. Commun.* **175**, 67 (2006).

[30] F. Birch, *Phys. Rev* **71**, 809 (1947).

[31] J. Wang, Y. Zhou, *Phys. Rev. B* **69**, 214111 (2004).

[32] K. Chinnadurai, B. Natesan, *Comput. Mater. Sci.* **188**, 110116 (2021).

[33] B. Shi, J. Li, C. Jin, J. Yang, C. Zhang, Y. Yan, Y. Wang, G. Zhang, *J. Magn. Magn. Mater.* **517**, 167383 (2021).

[34] R. Prakash, G. Suganya, G. Kalpana, *AIP Adv.* **12**, 055223 (2022).

[35] F.N. Gharbi, I.E. Rabah, M. Rabah, H. Rached, D. Rached, N. Benkhettou, F. Boukabrine, *SPIN* **10**, 2050002 (2020).

[36] J. Ma, L. Feng, R. Guo, Y. Liao, R. Khenata, G. Liu, L. Wang, *Materials* **10**, 1367 (2017).

[37] F. Mouhat, F.-X Coudert, *Phys. Rev. B* **90**, 224104 (2014).

[38] T. Yang, L. Hao, R. Khenata, X. Wang, *Materials* **11**, 2091 (2018).

[39] I. Galanakis, P. Mavropoulos, *Phys. Rev. B* **67**, 104417 (2003).

[40] C. Banerjee, N. Teichert, K.E. Siewierska, Z. Gercsi, G.Y.P. Atcheson, P. Stamenov, K. Rode, J.M.D. Coey, J. Besbas, *Nat. Commun.* **11**, 468 (2020).

[41] M. Ram, A. Saxena, A.E. Aly, A. Shankar, *RSC Adv.* **10**, 7661 (2020).

[42] S. Ghosh, S. Ghosh, *Phys. Status Solidi B* **256**, 1900039 (2019).

[43] G.Z. Xu, E.K. Liu, Y. Du, G.J. Li, G.D. Liu, W.H. Wang, G.H. Wu, *Europhys. Lett.* **102**, 17007 (2013).

[44] R. Mahat, S. Kc, U. Karki, J.Y. Law, V. Franco, I. Galanakis, A. Gupta, P. LeClair, *Phys. Rev. B* **104**, 014430 (2021).

[45] A.D. Becke, K.E. Edgecombe, *J. Chem. Phys.* **92**, 5397 (1990).

[46] A. Savin, B. Silvi, *Nature* **371**, 683 (1994).

[47] F. Fuster, A. Sevin, B. Silvi, *J. Phys. Chem. A* **104**, 852 (2000).

[48] S. Chen, Z. Ren, *Mater. Today* **16**, 387 (2013).

[49] Y. Nishino, S. Deguchi, U. Mizutani, *Phys. Rev. B* **74**, 115115 (2006).

[50] S. Mitra, A. Ahmad, S. Chakrabarti, S. Biswas, A. Kumar Das, *Phys. B Condens. Matter* **640**, 413878 (2022).

[51] B. Shi, J. Li, C. Jin, J. Yang, C. Zhang, Y. Yan, Y. Wang, G. Zhang, *J. Magn. Magn. Mater.* **517**, 167383 (2021).

[52] R. Prakash, G. Suganya, G. Kalpana, *AIP Adv.* **12**, 055223 (2022).

[53] I. Serhiienko, M. Parzer, F. Garmroudi, A. Novitskii, N. Tsujii, E. Bauer, Y. Grin, T. Mori, *J. Mater. Chem. A* **13**, 15268 (2025).

[54] A. Hzzazi, H. Alqurashi, E. Andharia, B. Hamad, M.O. Manasreh, *Crystals* **14**, 33 (2024).